


RESEARCH ARTICLE | APRIL 10 2024

## Using leeward air-blowing to alleviate the aerodynamic lateral impact of trains at diverse yaw angles

Special Collection: [Flow and Civil Structures](#)

Zi-Jian Guo; Zheng-Wei Chen   ; Zheng-Xin Che; Amir Bordbar; Yi-Qing Ni 



*Physics of Fluids* 36, 045121 (2024)

<https://doi.org/10.1063/5.0200310>



### Articles You May Be Interested In

On the active flow control in maglev train safety under crosswinds: Analysis of leeward suction and blowing action

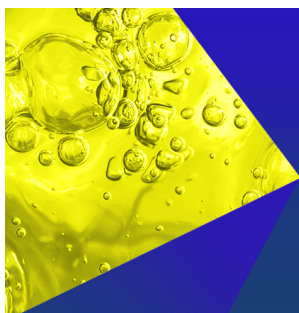
*Physics of Fluids* (September 2024)

Wake stabilization behind a cylinder by secondary flow over the leeward surface

*Physics of Fluids* (May 2022)

A novel vortex control method for improving anti-overturning performance of a high-speed train with leeward airbag structures under crosswinds

*Physics of Fluids* (June 2024)



**Physics of Fluids**  
Special Topics  
Open for Submissions

[Learn More](#)

# Using leeward air-blowing to alleviate the aerodynamic lateral impact of trains at diverse yaw angles

Cite as: Phys. Fluids **36**, 045121 (2024); doi: 10.1063/5.0200310

Submitted: 25 January 2024 · Accepted: 22 March 2024 ·

Published Online: 10 April 2024



View Online



Export Citation



CrossMark

Zi-Jian Guo,<sup>1,2</sup> Zheng-Wei Chen,<sup>1,2,a)</sup> Zheng-Xin Che,<sup>3</sup> Amir Bordbar,<sup>4</sup> and Yi-Qing Ni<sup>1,2</sup>

## AFFILIATIONS

<sup>1</sup>Department of Civil and Environmental Engineering, The Hong Kong Polytechnic University, Hong Kong, China

<sup>2</sup>National Rail Transit Electrification and Automation Engineering Technology Research Center (Hong Kong Branch), Hong Kong, China

<sup>3</sup>School of Rail-Transportation, Wuyi University, Jiangmen 529020, China

<sup>4</sup>School of Engineering, Computing and Mathematics, University of Plymouth, Plymouth PL4 8AA, United Kingdom

**Note:** This paper is part of the special topic, Flow and Civil Structures.

<sup>a)</sup>Author to whom correspondence should be addressed: [zhengwei.chen@polyu.edu.hk](mailto:zhengwei.chen@polyu.edu.hk)

## ABSTRACT

The safety risks of high-speed trains in crosswind environments escalate with increasing train speeds. The present study employs the improved delayed detached eddy simulation method based on the shear stress transport  $k-\omega$  turbulence model to evaluate an active control method targeting the reduction of lateral forces acting on the train. The effects of air blowing strategy on the leeward side of the train are examined considering different yaw angles and blowing speeds. The findings reveal that the active air blowing, mixed with the flow laterally downstream the train roof, induces the increase in the local turbulence and alters the surface pressure distribution. Within the investigated range of yaw angles, the active air blowing yields a lateral force reduction ranging from 1.0% to 8.8%. Varying the blowing speed can further decrease the lateral force of the entire train by 5.9% and 0.8% at yaw angles of 15° and 75°, respectively. The power invested in active blowing demonstrates maximum returns at a yaw angle near 45° while diminishing with increasing blowing speed.

Published under an exclusive license by AIP Publishing. <https://doi.org/10.1063/5.0200310>

## NOMENCLATURE

$A$	reference area	LWS	leeward side
$A_b$	blowing slots area	MOT	middle height of the train
$CFL$	courant number	$P$	absolute pressure
COR	center of the rail	$P_b$	Equivalent blowing power
$C_p$	coefficient of pressure	$P_0$	reference pressure
$C_y$	coefficient of lateral force	$\mathbf{q}$	heat flux
$C_z$	coefficient of lift force	$\mathbf{S}$	average strain rate tensor
$F_y$	lateral force of the train	SST	Shear Stress Transport
$F_z$	lift force of the train	$S_E$	energy source per unit volume
$F_{y-0}$	lateral forces acting on the origin train	TOR	top of the rail
$F_{y-1}$	lateral forces acting on the train with air-blowing	$U$	resultant velocity
$H$	height of the train	$u_t$	speed of the train
$\mathbf{I}$	unit tensor	$\mathbf{v}$	fluid velocity vector
IDDES	Improved Delayed Detached Eddy Simulation	WWS	windward side
$L$	total length of the train	$\alpha$	yaw angle
		$\Delta t$	time step for the transit simulation
		$\Delta F_y$	reduction in the lateral force

$\zeta_i$	reduction rate
$v_b$	blowing speed
$\rho$	density of the air
$\sigma$	power return coefficient
$\phi$	flow variables
$\bar{\phi}$	mean value of flow variables
$\phi'$	fluctuation component of flow variables

## I. INTRODUCTION

With the inherent advantages of speed, convenience, economy, and safety, trains play a pivotal role in facilitating the sustainable development of transportation.<sup>1–3</sup> However, as the number of train lines increases, their operating environment becomes progressively more intricate and unpredictable.<sup>4,5</sup> When trains run on open tracks, the presence of crosswinds exerts a substantial influence on the lateral aerodynamic characteristics, thereby affecting the train's operational stability and even giving rise to potential overturning incidents.<sup>6–9</sup> High-speed rail accidents stemming from crosswinds occur sporadically on a global scale.<sup>10</sup>

To ensure the safety of high-speed trains operating in crosswind environments, researchers have explored diverse methodologies. From a vehicle standpoint, the aerodynamic design of trains significantly governs the lateral force and rolling moment experienced by the train; the optimization of the train's geometric design represents an effective means of mitigating the lateral load imposed on the train.<sup>11–13</sup> However, the optimization possibilities for trains are often constrained within a limited range due to manufacturing processes and other disciplinary limitations. Consequently, when faced with stronger crosswinds, the installation of windproof barriers along the rail lines becomes an indispensable measure, safeguarding the secure operation of trains.<sup>14–18</sup>

While research on shape optimization and windproof barriers has matured considerably, it is gradually becoming inadequate in meeting the demands for increased train speeds under more intricate operating conditions. Consequently, there is a need to explore novel mitigation methods. Active flow field control technology, which has attained significant advancements in the aerospace sector, has demonstrated its efficacy in changing flow field structures and reducing aerodynamic forces acting on objects.<sup>19</sup> This technology has also found relevance in train aerodynamics, offering opportunities for research and improvement.<sup>1,20</sup> Chen *et al.*<sup>21</sup> studied the effect of air-blowing on the lateral aerodynamic force experienced by trains and achieved a reduction in the lateral rolling moment of 18.5% for the head car, 21.7% for the intermediate car, and 30.8% for the tail car. This study

demonstrates that air-blowing can reduce the lateral wind aerodynamic force on trains, but the blowing effect from each car and different blowing speeds are not studied. A sweeping jet utilized at the rear of a slanted-base cylinder was proved to be able to inject turbulence into the trailing vortex to induce the dispersion of the velocity gradient within the vortex, consequently leading to a reduction in its strength.<sup>22,23</sup> By injecting artificial turbulence that intersects with the naturally generated wake, a reactive force is generated on the vehicle through the action of the jet. Additionally, this injection of turbulence results in an augmentation of the surface pressure acting on the end plate. Collectively, these measures contribute to the attainment of net energy savings by optimizing the aerodynamic performance of the vehicle. The aerodynamic forces of a maglev train were actively controlled by arranging air holes in the transition zone from the streamlined section to the equal section.<sup>24</sup> The investigation encompassed both blowing and suctioning methods, evaluating their impact on train resistance. The results revealed that blowing, as an approach, led to an increase in train resistance, whereas suctioning demonstrated benefits in reducing resistance. Furthermore, the study delved into the effects of airflow direction and velocity, examining their influence on the overall outcome.

Different from the passive safety improvement method widely used on trains, this study applies an air blowing strategy on the leeward side (LWS) of the train to explore the application of active flow control on trains. The structure of the paper is as follows: the introduction of the train model, computational domain, mesh scheme, solving method, and validations are included in Sec. II; the results analysis among various yaw angles, and the mitigation efficiency assessment are included in Sec. III; the conclusion and summary are included in Sec. IV.

## II. METHODOLOGY

### A. Geometry model and computational domain

This study conducted numerical simulations using the CRH380A high-speed train model. The train model comprises three distinct cars, namely, the head, middle, and tail cars. Minor components such as headlights and door handles were excluded, while retaining essential geometric features such as train bogies and inter-carriage gaps. As depicted in Fig. 1(a), the top of the rail (TOR) is set as the reference plane  $Z = 0$ , while the plane at the center of the rail (COR) serves as the reference plane  $Y = 0$ . The train has a height of 3.7 m and a width of 3.38 m. Both the head and tail cars have a length of 26.5 m, whereas the intermediate car measures 25 m in length. Consequently, the total length of the train amounts to  $L = 78$  m. As shown in Fig. 1(b), the applied air-blowing slots for both the head car and the tail car measure

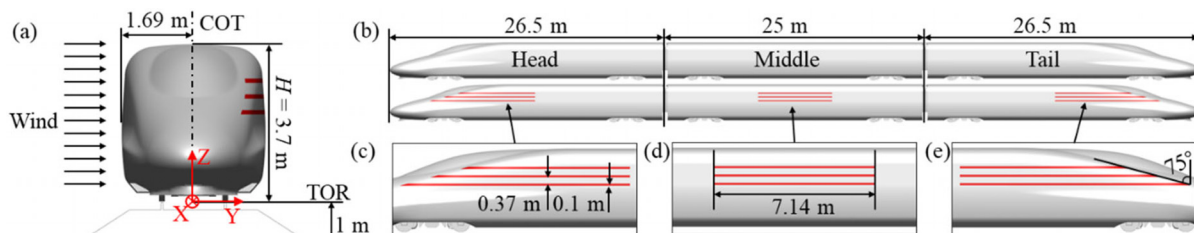


**FIG. 1.** Geometric model: (a) front view of the train and subgrade, (b) side view of the train, upper one is the prototype, and the lower one applies air-blowing slots, (c) zoomed details of air-blowing slots in the head car, (d) zoomed details of air-blowing slots in the intermediate car, and (e), zoomed details of air-blowing slots in the tail car.

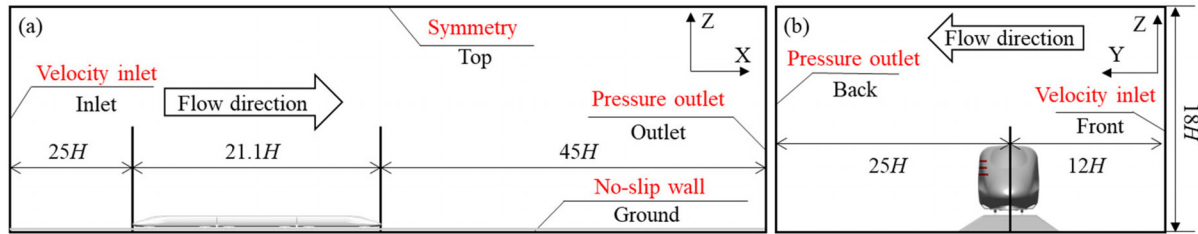


FIG. 2. Calculation domain and boundary conditions: (a) side view and (b) front view (not in scale).

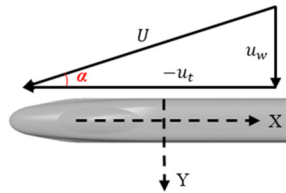


FIG. 3. Definition of the yaw angle  $\alpha$ .

10.2 m in length, while the intermediate car's air-blowing slot spans 7.14 m, and the width of each air-blowing slot is 0.1 m. Based on the position that can maximize the negative pressure distribution on the leeward side, the slots are positioned at an interval of 0.37 m from each other and the lowest one situates 0.2 m above the MOT (middle height of the train). In order to avoid any interference with the windshields of the head and tail cars, the lengths of the air-blowing slots in these cars are gradually adjusted with the height increases.

To conform the requirements of the employed turbulence model, the computational domain was 1/8 scaled down. The train height,  $H$ , corresponds to 0.4625 m, serving as the characteristic length in the present study. The dimensions of the computational domain are illustrated in Fig. 2. To guarantee the stability of the incoming flow, the distances from the front and side inlets to the train are set at  $25H$  and  $12H$ , respectively. Furthermore, to ensure the full development of the flow field around the train and minimize the influence of boundaries,

the distances from the rear and side outlets to the train are established as  $45H$  and  $25H$ , respectively. Sensitivity tests on the inlet and outlet distances from the train and blockage ratio have been performed, referring to the present study to demonstrate that these parameters do not affect the calculation results.<sup>25</sup>

Both the longitudinal and horizontal inlets were designated as velocity inlet boundaries with the components determined by various yaw angles ( $\alpha$ ), whose definition can be found in Fig. 3. The resultant velocity,  $U$ , approximately amounts to 60.92 m/s and the corresponding Reynolds number is calculated to be  $1.9 \times 10^6$ . The longitudinal and horizontal outlets were configured as zero-pressure outlets. The ground and the track were assigned as a moving no-slip wall, which moves with a speed same as the longitudinal component of  $-u_t$  to simulate the relative motion between the train and the track as well as the ground. The top surface of the computational domain was defined as a symmetrical wall. The boundary conditions of all air-blowing slots are set as the velocity inlet boundary conditions.

## B. Meshing strategy

To discretize the fluid zone in the computational domain, the trimmed cells were employed, including the prism layer grid attaching to the train's surface and the refined zones, which are depicted in Fig. 4. The total thickness of the prism layers attaching the surfaces is  $0.016H$ , comprising a total of 12 layers with a 1.2 growth rate. Given the complex and extensive nature of the flow fields on the leeward side of the train and in the wake region under crosswind conditions, the

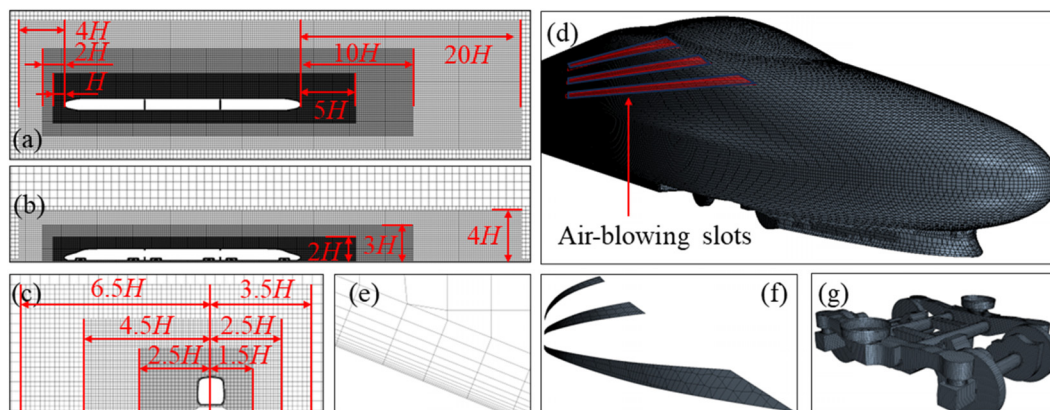


FIG. 4. The distribution of the cells on the (a) Z-slice of the domain, (b) the Y-slice of the domain, (c) the X-slice of the domain, (d) the head car, (e) the prism layers attaching the train surface, (f) air-blowing slots, and (g) bogie.

**TABLE I.** Mesh details for simulations using different mesh schemes.

Item	Coarse	Medium	Fine
Number of prism layers	12	12	12
Growth of thickness in prism layers	1.2	1.2	1.2
Surface mesh size of the train (mm)	10	5	2.5
Mean value of $\gamma^+$	1.8	1.8	1.8
Maximum skewness	0.69	0.74	0.78
Total number of cell ( $\times 10^6$ )	14.7	29.8	54.2

cells in these regions have been refined to obtain precise flow information. The refined zones have been divided into three sections with cell sizes of  $0.022H$ ,  $0.044H$ , and  $0.088H$ , respectively. The various levels of the refined zone can be observed in Figs. 4(a)–4(c), and the distribution of cells on the train surfaces and the prism layers is shown in Figs. 4(d)–4(g).

To ensure grid independence and optimize computational resources, three meshing schemes were employed in the present study. The cells in prism layers and refined zones remained consistent across all three schemes, while the grid size on the train's surface was varied to assess grid independence. The minimum grid sizes on the train surface for the three schemes were set at  $0.022H$  (Coarse),  $0.011H$  (Medium), and  $0.005H$  (Fine). The corresponding total number of grids for each scheme were  $14.7 \times 10^6$ ,  $29.8 \times 10^6$ , and  $54.2 \times 10^6$ , respectively. Details of the three mesh strategies can be found in Table I.

By comparing the pressure coefficient [ $C_p$ , defined as Eq. (8)] on the  $Y = 0$  section of the prototype case, as depicted in Fig. 5(a), it is evident that while the coarse case exhibits a consistent variation trend with the medium and fine results, there are noticeable differences in the  $C_p$  values. However, no significant difference can be observed between the results from medium and fine meshes. Similarly, when examining the lateral force coefficient [ $C_y$ , defined as Eq. (9)] calculated by the three meshes, as shown in Fig. 5(b), it is apparent that the  $C_y$  values for the head and tail cars in the coarse case are significantly lower than those in the medium and fine cases. Consequently, the medium meshing scheme is deemed sufficient to achieve the desired calculation accuracy, comparable to that of the fine mesh. Therefore, the medium mesh configuration is selected as the preferred scheme for

all cases in the present study. The grids representing the train surface, air-blowing slots, and bogie can be observed in Figs. 4(d), 4(f), and 4(g), respectively.

### C. Numerical solution scheme and verification

The Improved Delayed Detached Eddy Simulation (IDDES) method, based on the Shear Stress Transport (SST)  $k-\omega$  turbulence model, was utilized in this study, which has been extensively used in the field of high-speed trains<sup>26–30</sup> and was employed to simulate the flow field characteristics of a train running under crosswind conditions. As the most important laws in computational fluid dynamics (CFD),<sup>31,32</sup> the basic governing equations used can be seen as follows.

Mass conservation equation (continuity equation)

$$\frac{\partial \rho}{\partial t} + \nabla \cdot (\rho \mathbf{v}) = 0. \quad (1)$$

Momentum conservation equation [Navier–Stokes (NS) equation]

$$\frac{\partial (\rho \mathbf{v})}{\partial t} + \nabla \cdot (\rho \mathbf{v} \otimes \mathbf{v}) = \nabla \cdot \boldsymbol{\sigma} + \mathbf{f}_b. \quad (2)$$

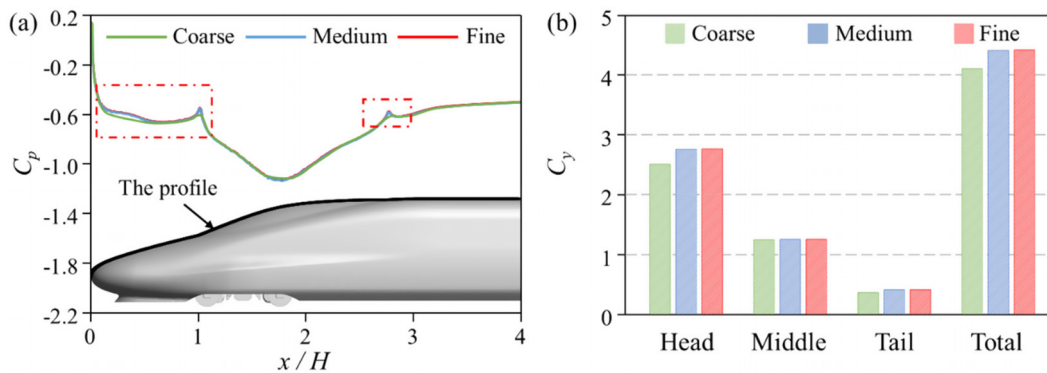
Energy conservation equation

$$\frac{\partial (\rho E)}{\partial t} + \nabla \cdot (\rho E \mathbf{v}) = \mathbf{f}_b \cdot \mathbf{v} + \nabla \cdot (\mathbf{v} \cdot \boldsymbol{\sigma}) - \nabla \cdot \mathbf{q} + S_E, \quad (3)$$

where  $\rho$  is the air density;  $\mathbf{v}$  is the fluid velocity vector, representing the velocity components in the three directions of  $x$ ,  $y$ , and  $z$ , respectively.  $\otimes$  is the Kronecker product,  $\mathbf{f}_b$  is the resultant force of various physical forces (such as gravity and centrifugal force) acting on the unit volume of the continuum, and  $\boldsymbol{\sigma}$  is the stress tensor.  $E$  is the total energy per unit mass,  $\mathbf{q}$  is the heat flux, and  $S_E$  is the energy source per unit volume.

For the  $k-\omega$  equation employed in the study, to obtain the Reynolds-averaged NS equation requires decomposing each solution variable  $\phi$  in the instantaneous NS equation into its mean value  $\bar{\phi}$  and its fluctuation component  $\phi'$

$$\phi = \bar{\phi} + \phi'. \quad (4)$$

**FIG. 5.** The comparison of the results from three meshing in terms of (a)  $C_p$  of  $Y = 0$  profile along the upper surface of the train and (b)  $C_y$  of each car and the total.



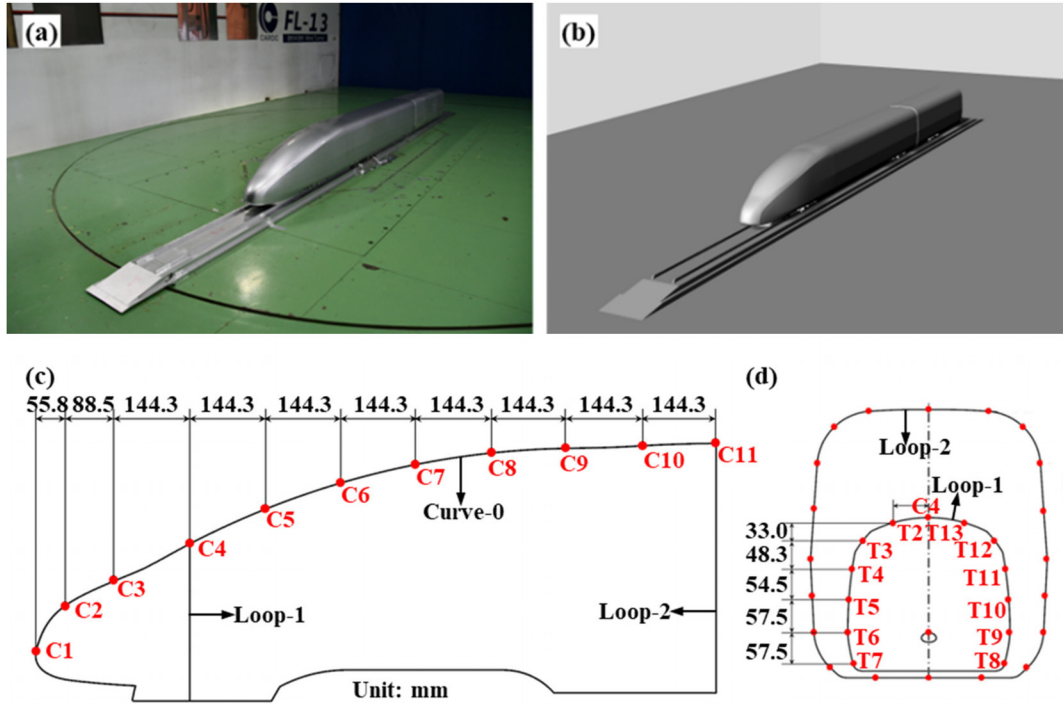


**FIG. 6.** Verification of the numerical scheme using the wind tunnel test: (a) train model used in the wind tunnel test, (b) train model used in numerical simulation, (c) side view of the interested profile, and (d) front view of the interested profile.

Inserting the decomposed solution variables into the Navier-Stokes equations produces an equation for the mean quantity. The average mass and momentum transfer equation can be written as

$$\frac{\partial \rho}{\partial t} + \nabla \cdot (\rho \bar{\mathbf{v}}) = 0, \quad (5)$$

$$\frac{\partial}{\partial t}(\rho \bar{\mathbf{v}}) + \nabla \cdot (\rho \bar{\mathbf{v}} \otimes \bar{\mathbf{v}}) = -\nabla \cdot \bar{\mathbf{p}}\mathbf{I} + \nabla \cdot (\mathbf{T} + \mathbf{T}_t) + \mathbf{f}_b. \quad (6)$$

It is difficult to model  $\mathbf{T}_t$  based on the average flow rate to close the control equation, so an eddy viscosity model based on the similarity between the molecular gradient diffusion process and turbulent motion is introduced. The Reynolds stress tensor can be mapped as a function of the mean flow using the turbulent eddy viscosity  $\mu_t$ . The most widely used model is the Boussinesq approximation

$$\mathbf{T}_t = 2\mu_t \mathbf{S} - \frac{2}{3}(\mu_t \nabla \cdot \bar{\mathbf{v}})\mathbf{I}, \quad (7)$$

where  $\phi$  represents the velocity component, pressure, energy, or component concentration.  $\bar{\mathbf{v}}$  is the average velocity, respectively,  $\mathbf{I}$  is the unit tensor, and  $\mathbf{S}$  is the average strain rate tensor.

The time step ( $\Delta t$ ) was set to  $8 \times 10^{-5}$  s to maintain a Courant number [(Courant-Friedrichs-Lewy (CFL))] of no more than 1. A total of 20 000 steps of transient calculation and 10 000 steps of time-averaged processing were performed to ensure the complete development of the flow field and the accuracy of the time-averaged results. Each time step needs 30 iterations, with a residual of  $10^{-5}$ . Sensitivity

tests on the time step have also been performed to demonstrate that the discreteness of time does not affect the calculation results.

Data from a wind tunnel test conducted by Huo *et al.*<sup>33</sup> was utilized to validate the feasibility of the numerical solution results. Both the wind tunnel test and the simulation employed 1:8 scaled one-and-a-half train models, as depicted in Figs. 6(a) and 6(b). According to the test situation, the yaw angle was set at  $30^\circ$ , and the inlet flow velocity was 45 m/s. Further details of the wind tunnel test can be found in the referenced study. The side force coefficient ( $C_y$ ) and the lift force coefficient [ $C_z$ , defined as Eq. (10)] of the head car are compared between the wind tunnel test and the simulation, as presented in Table II, which shows that the differences in  $C_y$  and  $C_z$  between the two cases were both below 4%. Values of  $C_p$  along Curve-0 and Loop-1 shown in Figs. 6(c) and 6(d) obtained from the test and simulation are presented in Fig. 7, which exhibits a good agreement. In conclusion, the numerical scheme adopted in the current study has been demonstrated reliable in predicting the aerodynamic performance of trains.

**TABLE II.** Aerodynamic coefficients obtained from the wind tunnel test and simulation.

Item	$C_y$	$C_z$
Wind tunnel test <sup>33</sup>	4.2757	4.5266
Numerical simulation	4.2439	4.3762
Error	0.75%	3.44%

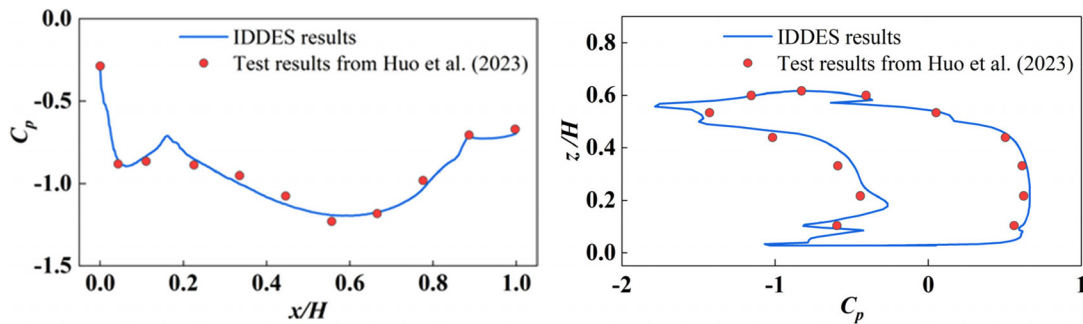


FIG. 7. The value of  $C_p$  obtained from the wind tunnel test and numerical result: (a) Curve-0 and (b) Loop-2.

### III. RESULTS AND DISCUSSION

#### A. Air-blowing effectiveness in different yaw angles

As illustrated in Fig. 8, the longitudinal middle positions of the air-blowing slots on the head car, intermediate car, and tail car are designated as X1, X2, and X3, respectively. To establish a clear reference, the longitudinal plane of symmetry of the train serves as the dividing line, where the side directly exposed to the crosswind is referred to as the windward side (WWS), while the opposite side is termed the leeward side (LWS). By employing these specific designations, a comprehensive investigation can be conducted to assess the impact of the air-blowing mechanism on the surface pressure characteristics within the designated areas.

In addition, the dimensionless coefficients of the lateral force ( $C_y$ ), lift force ( $C_z$ ), and their respective reduction rate  $\zeta_i$  attributed to the blowing method are defined below

$$C_p = \frac{P - P_0}{0.5\rho U^2}, \quad (8)$$

$$C_y = \frac{F_y}{0.5\rho U^2 A}, \quad (9)$$

$$C_z = \frac{F_z}{0.5\rho U^2 A}, \quad (10)$$

$$\zeta_i = \frac{C_i - C_{i0}}{C_{i0}}, \quad (11)$$

where the pressure  $P$  and  $P_0$ , the lateral force  $F_y$ , and the lift force  $F_z$  were outputted by the solver; the air density  $\rho = 1.225 \text{ kg/m}^3$  was applied; the reference area  $A$  measures  $11.22 \text{ m}^2$  for full-scale size and  $0.1753 \text{ m}^2$  under an 1/8 scaling for numerical study. The  $i$  in Eq. (11) represents  $y$  and  $z$ . Note that the lateral force metrology differed by the blowing slots has been considered and compensated in terms of the pressure lateral force, frictional lateral force, and the impulse due to blowing.

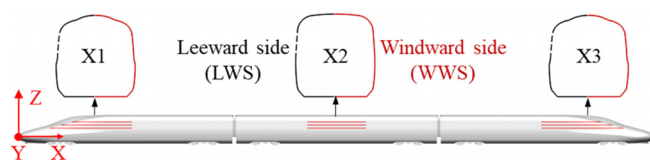
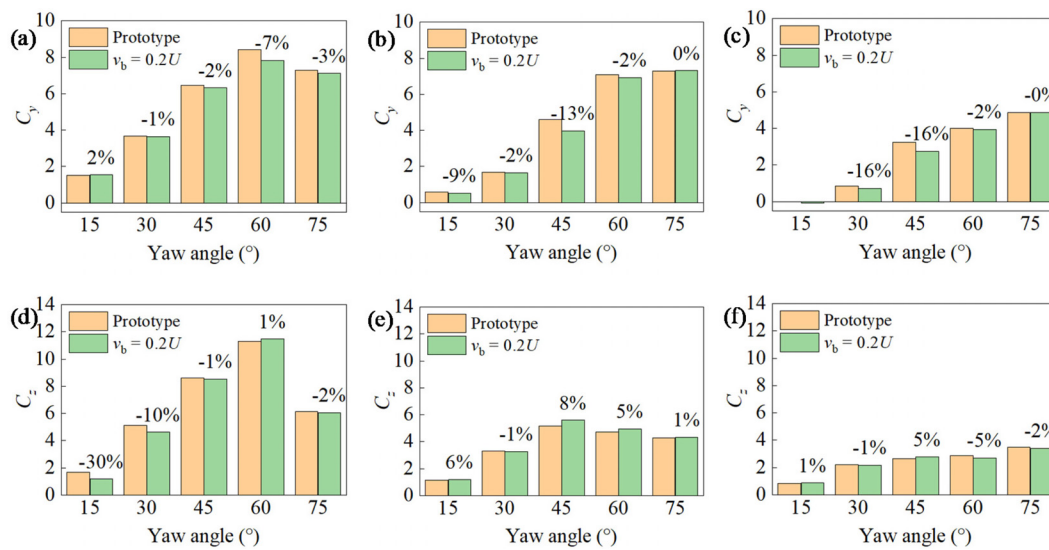


FIG. 8. Positions and profile of X1, X2, and X3 cross sections.

Figure 9 exhibits the aerodynamic lateral force coefficients [(a)–(c)] and lift force coefficients [(d)–(f)] acting on the leading car, intermediate car, and tail car, respectively, for yaw angles ranging from  $15^\circ$  to  $75^\circ$  in  $15^\circ$  increments. The results are obtained from the prototype train and that applying the air-blowing from the slots shown in Fig. 2 with a blowing speed ( $v_b$ ) of  $0.2U$  along the normal direction. To simultaneously observe the effects of the yaw angle and the car position, the unified ranges for lateral and lift forces values are utilized. The discrepancy  $\zeta_i$  between the two conditions is indicated as a label on the corresponding bar representing the blowing results. According to the coupled aerodynamic behavior of the train and crosswind, the lateral force experienced by the leading car, intermediate car, and tail car decreases as the position progresses downstream. As the yaw angle increases, the lateral force on the leading car initially rises and subsequently declines, whereas the lateral force on the intermediate car and tail car continues to increase. In most cases, the air-blowing slots on the leeward side have demonstrated their capability to reduce the aerodynamic lateral forces acting on each car. The extent of reduction is contingent upon the vehicle position and yaw angle. Overall, for yaw angles ranging from  $15^\circ$  to  $75^\circ$  in  $15^\circ$  increments, the total lateral force reductions of a whole train achieved by applying the air blowing strategy are 4.7%, 3.1%, 8.8%, 4.3%, and 1.0%, respectively.

From Figs. 9(d)–9(f), it can be observed that the leading car experiences the highest aerodynamic lift force, followed by the intermediate car. The lift force initially increases and then decreases as the yaw angle increases. Unlike the lateral force, the air-blowing slot on the leeward side is less effective in mitigating the aerodynamic lift force experienced by the vehicle. Consequently, more situations about lift force increase are observed on the vehicles. However, based on previous research,<sup>18</sup> the lift force does not significantly impact the train's overturning compared to the lateral force; the primary parameter influencing overturning is the coefficient of the lateral force. As a result, the lift force results presented here serve as the supplementary analysis of the vehicle's aerodynamics and do not serve as a basis for determining the impact of crosswind stability on the vehicle.

The aerodynamic force is the integral result of the aerodynamic pressure on the train surface. Figure 10 shows the pressure distribution on the leeward side surfaces of the leading car, the intermediate car, and the tail car at different wind direction angles with and without applying the air blowing strategy to explore how the air blowing change of the local and local pressure distribution further affects the vehicle's lateral forces. Due to the large difference in pressure on trains



**FIG. 9.** Aerodynamic coefficients and their reduction rate on each car in various yaw angles: (a)  $C_y$  of the head car, (b)  $C_y$  of the intermediate car, (c)  $C_y$  of the tail car, (d)  $C_z$  of the head car, (e)  $C_z$  of the intermediate car, and (f)  $C_z$  of the tail car.

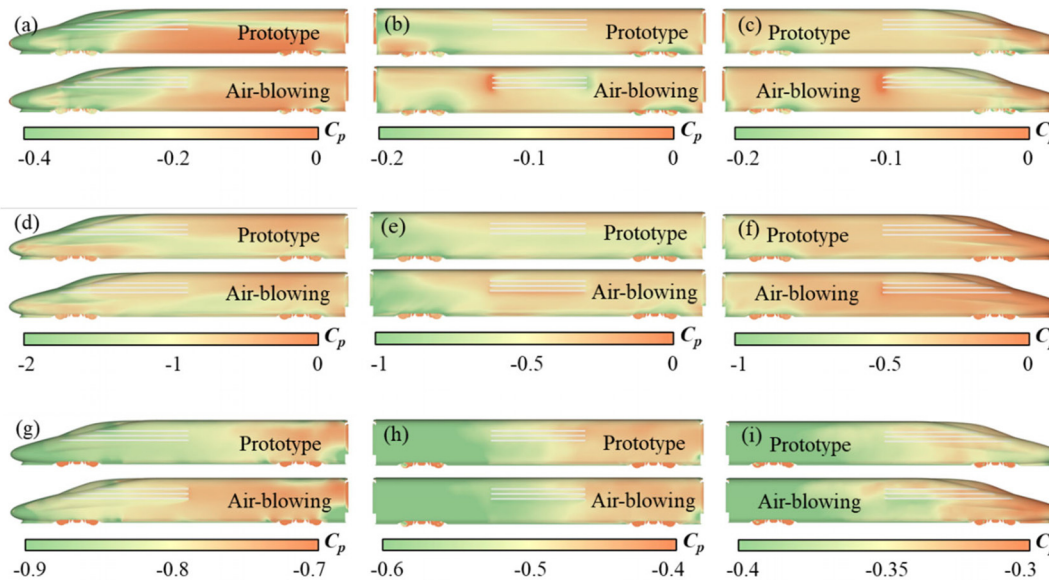


**FIG. 10.** Pressure distribution on LWS of the train in various yaw angles: (a)  $\alpha = 15^\circ$ , head car, (b)  $\alpha = 15^\circ$ , intermediate car, (c)  $\alpha = 15^\circ$ , tail car, (d)  $\alpha = 45^\circ$ , head car, (e)  $\alpha = 45^\circ$ , intermediate car, (f)  $\alpha = 45^\circ$ , tail car, (g)  $\alpha = 75^\circ$ , head car, (h)  $\alpha = 75^\circ$ , intermediate car, and (i)  $\alpha = 75^\circ$ , tail car. Colored by each-fitted range; the upper of each figure represents the prototype.

under the influence of yaw angles, which even occurs on different vehicles under the same yaw angle, the most appropriate pressure ranges are applied to each subfigure to clearly show the differences in flow behavior. The results for three yaw angles are shown to represent different composite relationships between the train speed and the crosswind speed, as presented in Fig. 3. As shown in Fig. 10(a), before the area that the blowing can affect, the pressure distribution of the two cases does not differ. The difference starts from the longitudinal

position of half the length of the blowing slots: for the pretotype train, a more obvious pressure boundary appears here, where the blowing postpones it to the tail of the blowing slots. However, the scope of the blowing groove is limited; it cannot suppress the pressure at a lower position far away from it like it can do at its height. Therefore, for these areas, the retardation effect is less obvious: a demarcation originating from the rear of the bogie compartment and representing a higher surface pressure gradient develops downstream and above. On the



leeward side of this car, although the air blowing relieved the negative pressure in the rear half of the car, it caused more large negative pressure regions to be maintained on the front half of the car, which is not conducive to reducing the pressure-caused lateral force on the head car. As shown in Figs. 9(b) and 9(c), the airflow flowing out normal to the leeward side of the train directly impacts the incoming flow around the train, causing local accumulation at the upstream end of the air-blowing slot, increasing the small negative pressure area, and reducing the large negative pressure area on the leeward side. The reduction of the lateral force is effectively suppressed; see Fig. 9(b). This logic of mitigating the vehicle lateral force is common to all trains in the picture. Different yaw angle increases may offset this active regulation of the pressure area, resulting in different changes in the lateral force. Generally, the change in pressure on the leeward side of the leading car is the most significant.

The influence of air blowing on flow behavior can be quantitatively analyzed by examining the pressure distribution across the cross section of the car body. Figures 11(a)–11(c) depict the pressure coefficient ( $C_p$ ) on the leeward side of three profiles, namely, X1, X2, and X3, while Figs. 11(d)–11(f) represent the windward side. Different colors in the figures indicate the calculation results at various yaw angles, illustrating the distinct effects of yaw angles on the pressure

distribution of the train and the effectiveness of air blowing. The three horizontal occlusions highlighted in light green correspond to the locations of the three air-blowing slots. The filled regions between the data points visually demonstrate the changes in pressure coefficient resulting from the air blowing strategy. The leeward side, which is of particular interest in this study, is predominantly characterized by negative pressure. When the yaw angle is  $45^\circ$  (as indicated by the red line and red filling in the figure), the pressure variation range along each contour is the largest, corresponding to the maximum range displayed in the color bar of Fig. 10. The impact of blowing air is also most pronounced at this yaw angle. On the leading car, the active normal airflow increases the pressure below  $0.3z/H$  and significantly reduces the pressure coefficient above it. On the intermediate car and the tail car, except for the transitional region between the roof and leeward side, the airflow effectively alleviates the negative pressure on the LWS surface. Consequently, the effective reduction in the lateral force for the intermediate car and tail car reaches 13% and 16%, respectively. When the yaw angle is  $15^\circ$ , the negative pressure on the leeward side of the leading car increases from the bottom to the top but remains at a relatively constant small negative pressure value on the cross section of the intermediate car and tail car. The air blowing slows down the negative pressure increase in certain areas on the leeward side of the leading car

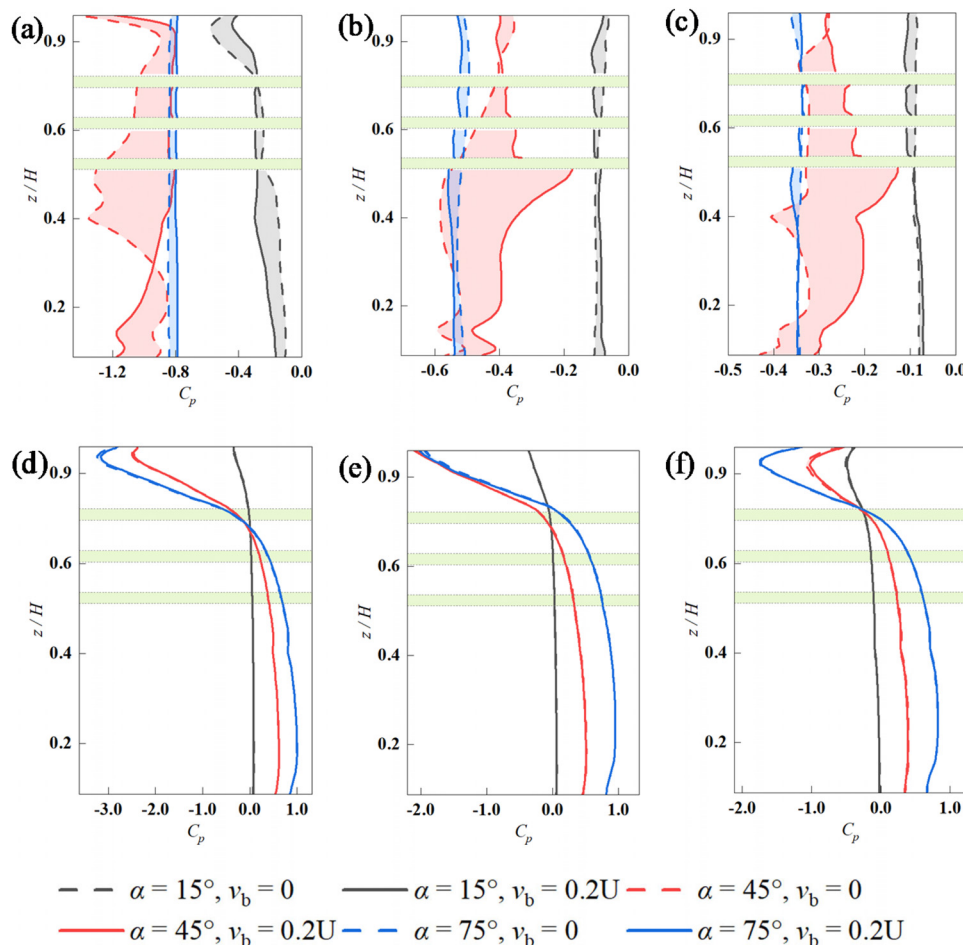


**FIG. 11.** Pressure distribution on the profiles of cross sections of the train: (a) LWS at X1, (b) LWS at X2, (c) LWS at X3, (d) WWS at X1, (e) WWS at X2, and (f) WWS at X3.

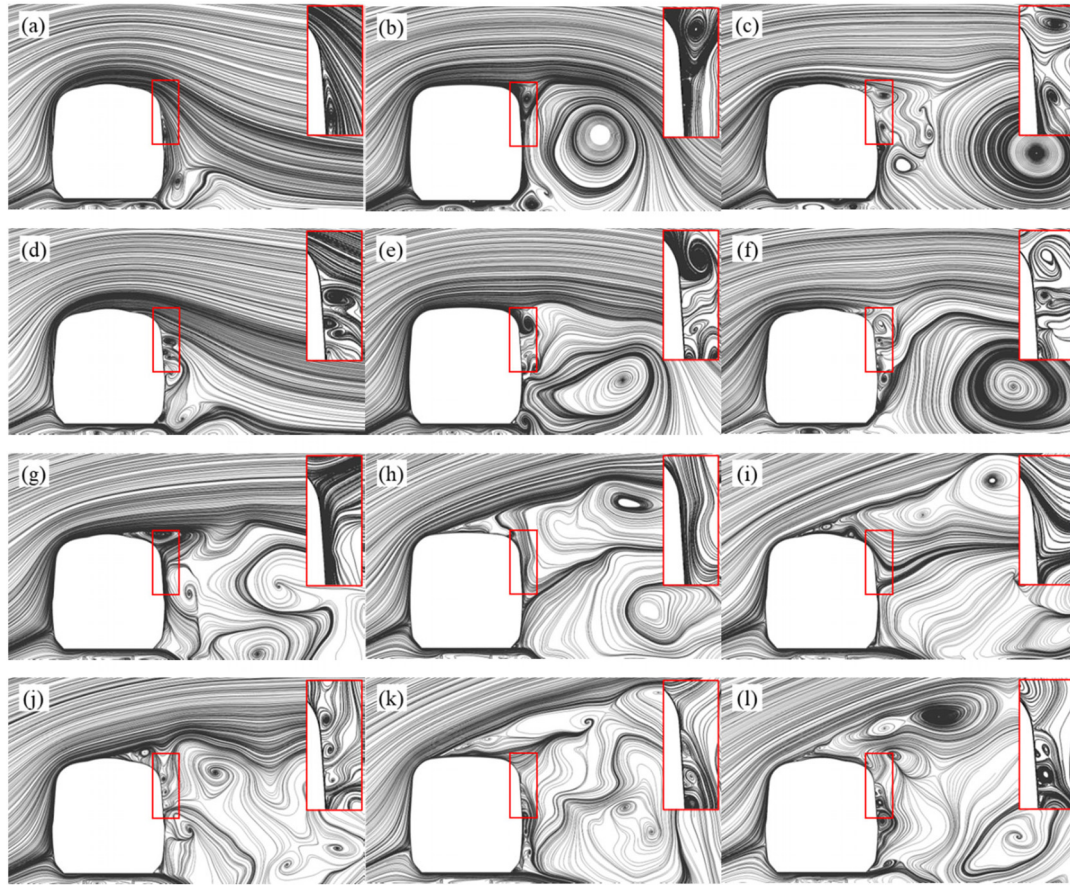


**FIG. 12.** Streamlines projected to X-slices showing the vortex shedding and wake: (a)  $\alpha = 15^\circ$ , prototype, X1, (b)  $\alpha = 15^\circ$ , prototype, X2, (c)  $\alpha = 15^\circ$ , prototype, X3, (d)  $\alpha = 15^\circ$ ,  $v_b = 0.2U$ , X1, (e)  $\alpha = 15^\circ$ ,  $v_b = 0.2U$ , X2, (f)  $\alpha = 15^\circ$ ,  $v_b = 0.2U$ , X3, (g)  $\alpha = 75^\circ$ , prototype, X1, (h)  $\alpha = 75^\circ$ , prototype, X2, (i)  $\alpha = 75^\circ$ , prototype, X3, (j)  $\alpha = 75^\circ$ ,  $v_b = 0.2U$ , X1, (k)  $\alpha = 75^\circ$ ,  $v_b = 0.2U$ , X2, and (l)  $\alpha = 75^\circ$ ,  $v_b = 0.2U$ , X3.

while influencing the negative pressure at other heights. The impact on the intermediate car and tail car is opposite, resulting in an increase in positive pressure at higher heights. When the yaw angle is  $75^\circ$ , the negative pressure coefficient on the leeward side of each car section exhibits a more stable change along the height compared to smaller yaw angles. Blowing air consistently weakens the negative pressure in the leeward side region of the leading car but slightly increases the negative pressure in the leeward side area of the intermediate car and tail car.

The pressure distribution and changes on the windward side shown in Figs. 11(d)–11(f) show that the air-blowing slots on the leeward side basically do not change the pressure distribution pattern and value on the windward side, especially for the lower heights, while it can be slightly affected by air-blowing on the transition area from roof to the leeward side.

Moreover, by confining the streamlines located on domain slices X1, X2, and X3 (Fig. 12), we can capture the variations in flow patterns that arise from the blowing strategy at different yaw angles, specifically in terms of vortex shedding and the wake. The main portion of the figure illustrates the overall evolution of the vehicle's lateral wake while also emphasizing a specific area around the blowing slots (marked with a red rectangle) that exhibits localized and subtle flow behavior.

This region is enlarged and inserted in the upper right corner of each image. A fundamental observation is that the introduction of air-blowing completely alters the flow structure surrounding the transition region from the top to the Lee-Ward Side (LWS) of the prototype vehicle, resulting in increased turbulence. Consequently, the large-scale vortices in the wake undergo both longitudinal and lateral deformation. The discrepancies in surface pressure on the car body depicted in Fig. 11 can be attributed to the interaction between the active normal airflow on the leeward side and the separated airflow bypassing the roof. This interaction disrupts the original separation and reattachment mode, leading to chaotic flow behavior. Furthermore, the local small-scale flow reconstruction near the air-blowing slots subsequently modifies the surface pressure distribution, resulting in comprehensive and distinct pressure changes dependent on the yaw angle and vehicle position.

Considering the potential impact of air blowing on the transition region between the top of the train and the leeward side area, Fig. 13 presents the distribution of pressure coefficients on the longitudinal symmetry plane ( $Y=0$ ) of the train, comparing the prototype case with the application of the air blowing strategy. The red areas on the train model represent the air blowing grooves, and the green bands in the figure indicate the longitudinal positions of these slots. Across the

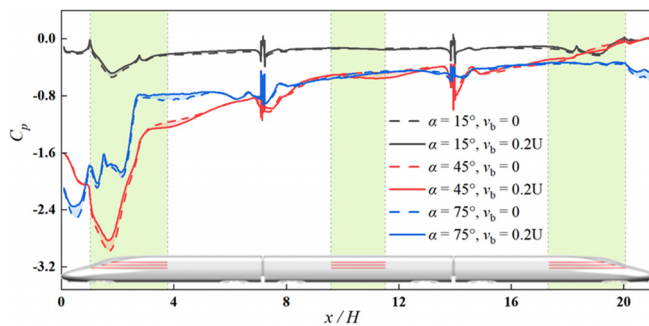


FIG. 13. Pressure distribution on the  $Y=0$  profile along the upper surface of the train.

three presented yaw angles, the air-blowing slots induce a reduction in pressure in and near their respective longitudinal positions. When the yaw angle is  $45^\circ$ , it leads to an increase in negative pressure within certain ranges. This observation aligns with the pressure values indicated in Figs. 10 and 11, corresponding to the differences in streamlines above the longitudinal symmetry plane in Fig. 12. However, it should be noted that the pressure changes caused by the air-blowing are not discernible at locations further away from the air-blowing slots.

At a yaw angle of  $15^\circ$ , particles emitted from a vertical line upwind the nose of the head car are tracked three-dimensionally around the train, which is shown in Fig. 14. The streamlines of the prototype are represented in black, while the streamlines corresponding to the application of leeward blowing are depicted in red. Two specific areas, labeled as Region A and B, are of particular interest: Region A can be regarded as an indirect effect on the flow, indicating that the streamlines after applying air blow develop a wider lateral and vertical range at the same longitudinal position, while Region B can be regarded as the direct influence of the air blowing, causing the vortex flow that should be close to the leeward side surface of the vehicle to be delayed downstream, proving the driving effect of the air blowing on the flow.

### B. Air-blowing effectiveness with different blowing speeds

Based on the aforementioned findings, implementing an air blowing strategy along the normal direction on the leeward side of the

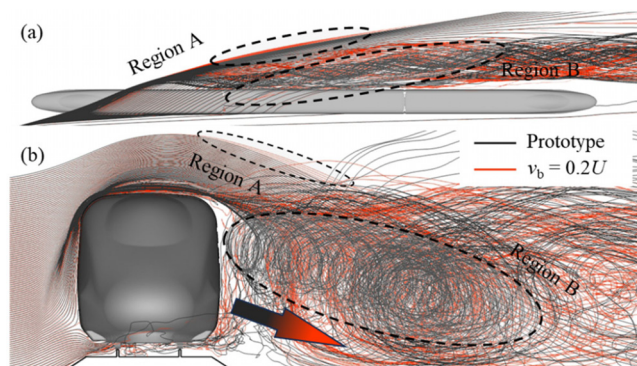


FIG. 14. 3D streamlines derived from a vertical emission near the head nose: (a) top view and (b) front view.

train can effectively alter the flow dynamics near the air-blowing slots. This, in turn, impacts the pressure distribution on both the top of the car body and the leeward side surface, resulting in a significant reduction in aerodynamic lateral forces acting on the train. Consequently, the risk of train overturning in crosswind conditions can be mitigated. Furthermore, the study extended its investigation to examine the variations in aerodynamic forces experienced by each section of the train when the air-blowing slots generate normal airflow at different velocities, as illustrated in Fig. 15. Numerical simulation results obtained at three distinct blowing speeds,  $0.1U$ ,  $0.2U$  (utilized in Sec. III A analysis), and  $0.3U$ , were compared with the prototype case. For a train operating at a yaw angle of  $15^\circ$ , as the air-blowing speed increases, the initially increasing effect on the lateral force of the leading car transitions into an effective reduction. Additionally, the inhibitory impact on the lateral force of the intermediate car and the tail car, as well as the lift force of the leading car, gradually diminishes. Eventually, at an air blowing speed of  $0.3U$ , these forces reach a level nearly equivalent to those experienced by the prototype. The total lateral force reductions of a whole train achieved by applying the air blowing strategy are 2.3%, 4.7%, and 8.2%, respectively. In the case of a train operating at a yaw angle of  $75^\circ$ , blowing air at a speed of  $0.2U$  exhibits minimal changes in both the lateral force and lift force of the vehicle, regardless of whether it results in an increase or decrease in the forces. The total lateral force reductions of the whole train achieved by applying the air blowing strategy are 1.1%, 1.0%, and 0.3%, respectively.

Figure 16 illustrates the pressure distribution on the leeward side surface of each car when generating normal airflow at different speeds over the blowing slots to examine the influence of blowing speed on the pressure distribution, as it directly affects the aerodynamic lateral forces on the vehicle, as depicted in Figs. 15(a)–15(c). The analysis focuses on two yaw angles,  $15^\circ$  and  $75^\circ$ , representing cases where the train speed and crosswind speed dominate the resultant wind speed, respectively. For the train operating at a yaw angle of  $15^\circ$ , increasing the blowing speed leads to a greater area with small negative pressures and a smaller area with large negative pressures on the leeward side surface. Notably, the regions most affected by the blowing effects are the vicinity of the head car's leeward blowing slot location and the upstream end of the intermediate and trailing cars' blowing slots. These regions experience significant changes in pressure distribution due to the blowing effects. Consequently, the lateral force component influenced by the pressure difference decreases, resulting in a decrease in lateral force with increasing blowing speed, as observed in Figs. 15(a)–15(c). In the case of trains operating at a yaw angle of  $75^\circ$ , blowing systematically modifies the pressure distribution on the leeward side of the head car in a pattern independent of the blowing speed. At a blowing speed of  $0.2U$ , there is a larger region of greater negative pressures above the second bogie, leading to a reduced lateral force of only 2.6%, which is lower compared to blowing speeds of  $0.1U$  and  $0.3U$ , where the reductions are 3.1% and 3.2%, respectively. Regarding the intermediate car, although there is a decrease in the area of small negative pressure regions downstream of the leeward side with increasing blowing speed, more large negative pressure regions are present near the upstream end of the blowing slot when  $v_b = 0.2U$ . Consequently, the vehicle experiences a lateral force closer to that of the prototype, with a reduction of only 0.2%. As for the tail car, although the small negative pressure region is largest at a blowing speed of  $0.2U$ , there is still a noticeable distribution of a slightly larger negative pressure under the



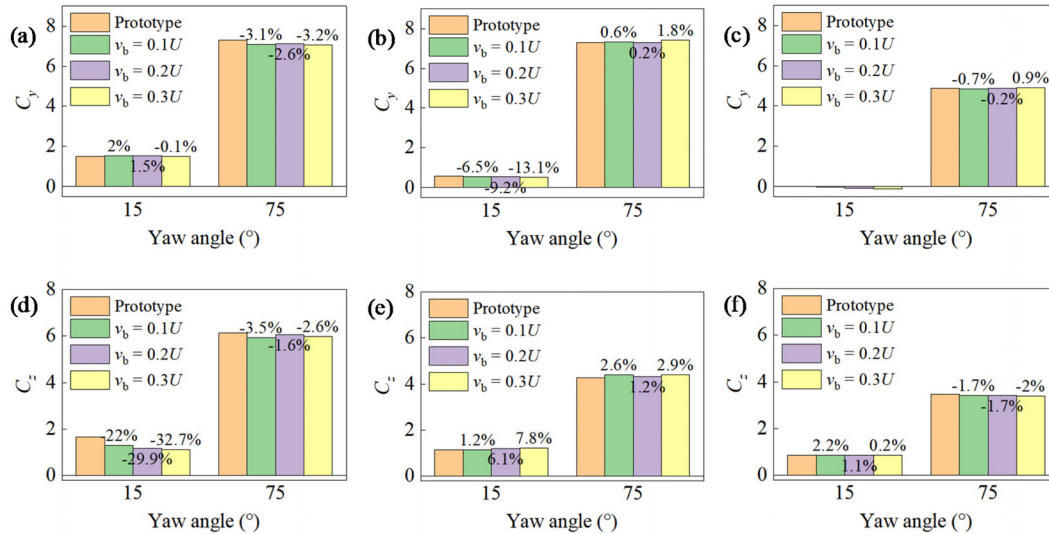


FIG. 15. Aerodynamic coefficients and their reduction rate on each car using various air-blowing speeds: (a)  $C_y$  of the head car, (b)  $C_y$  of the intermediate car, (c)  $C_y$  of the tail car, (d)  $C_z$  of the head car, (e)  $C_z$  of the intermediate car, and (f)  $C_z$  of the tail car.

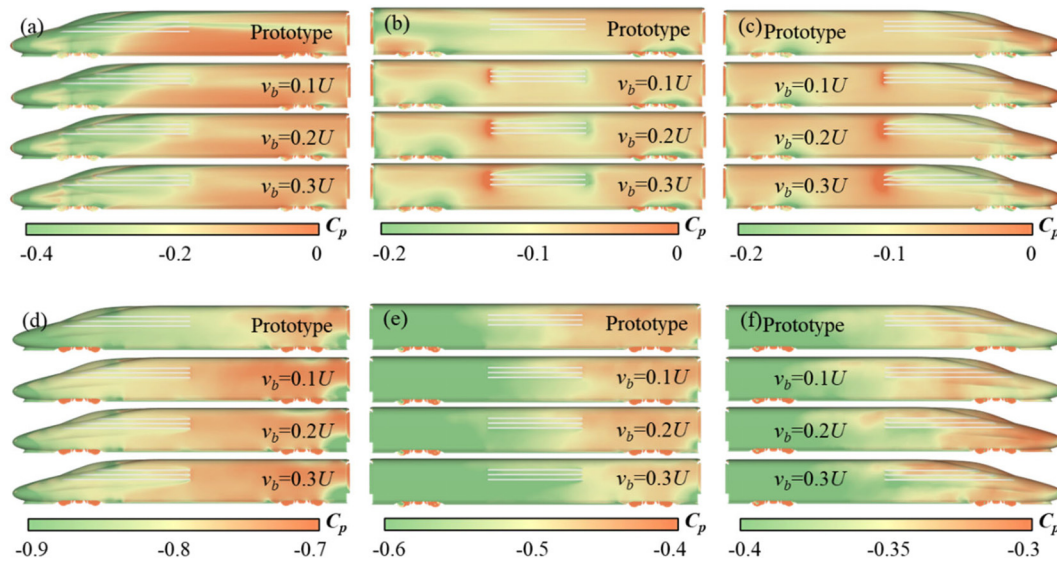


FIG. 16. Pressure distribution on LWS of the train using various air-blowing speeds: (a)  $\alpha = 15^\circ$ , head car, (b)  $\alpha = 15^\circ$ , intermediate car, (c)  $\alpha = 15^\circ$ , tail car, (d)  $\alpha = 75^\circ$ , head car, (e)  $\alpha = 75^\circ$ , intermediate car, and (f)  $\alpha = 75^\circ$ , tail car. Colored by each-fitted range; subfigures from up to down means prototype,  $v_b = 0.1U$ ,  $v_b = 0.2U$ , and  $v_b = 0.3U$ .

first half of the blowing slot compared to a blowing speed of  $0.1U$ . Hence, the suppression of lateral force is not as effective as at  $0.1U$ . When the blowing speed is  $0.3U$ , the small negative pressure region decreases, while the large negative pressure region near the blowing slot increases, ultimately resulting in an overall increase in lateral force.

Figure 17 presents the profile of pressure coefficients at three positions, namely, X1, X2, and X3, when different blowing speeds are applied to the leeward side of the train. Due to the absence of surface, the data on the blowing slots is discontinuous. When the train operates with a yaw angle of  $15^\circ$ , the pressure distribution on the leeward side

of the head car exhibits a significant span, with a fluctuation range from 0 to  $-0.6$ . The implementation of air blowing reduces this fluctuation to a range of  $-0.1$  to  $-0.5$ . Below and at the height of the blowing slot, the blowing air increases the negative pressure on the train surface, while above the blowing slot, it has the opposite effect. Among the different air blowing speeds, the pressure distribution at a blowing speed of  $0.1U$  closely resembles that of the prototype, while the results for  $0.2U$  and  $0.3U$  are similar. Regarding the intermediate car and tail car, blowing slightly decreases the pressure below the slots and increases the pressure above it. Below the blowing slot, the pressure



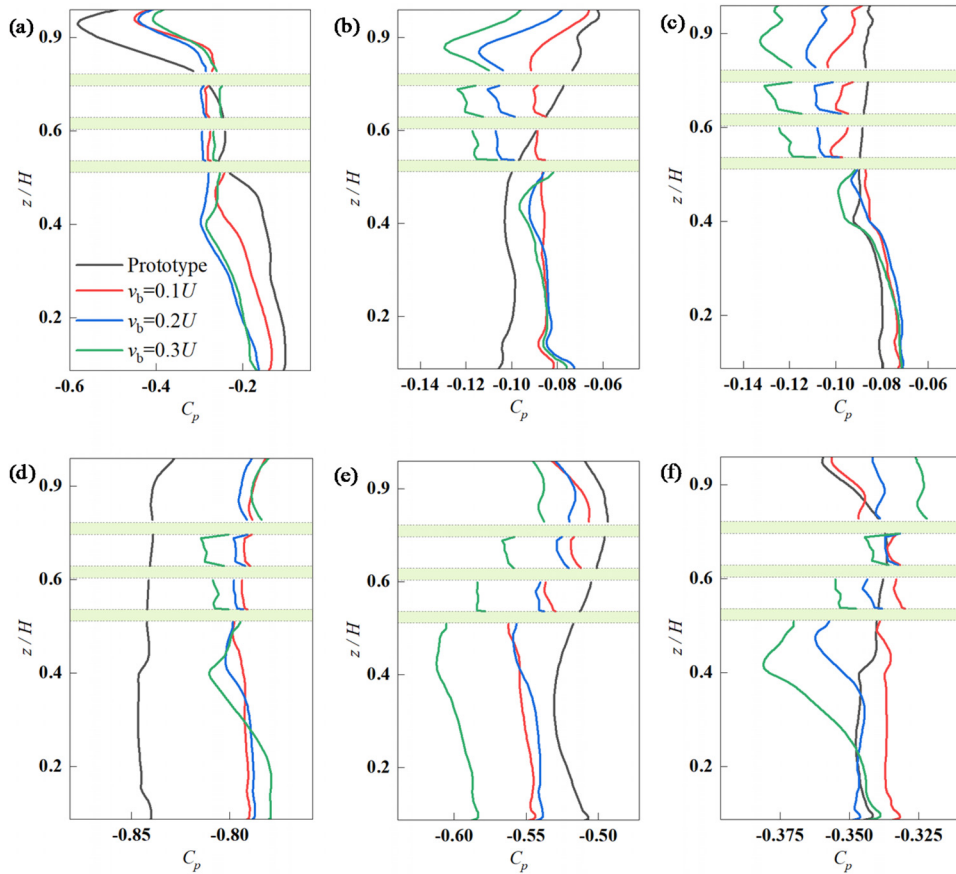


**FIG. 17.** Pressure distribution on the LWS profiles of cross sections of the train: (a)  $\alpha = 15^\circ$ , X1, (b)  $\alpha = 15^\circ$ , X2, (c)  $\alpha = 15^\circ$ , X3, (d)  $\alpha = 75^\circ$ , X1, (e)  $\alpha = 75^\circ$ , X2, and (f)  $\alpha = 75^\circ$ , X3.

difference caused by the blowing speed is not prominent, but it increases with the blowing speed above the slots. When the train operates with a yaw angle of  $75^\circ$ , the pressure coefficient span at these positions is less than  $15^\circ$ , and the effect of air blowing on the head car appears to be more systematic. The negative pressure is attenuated across the entire height range, and the minimum blowing speed provides the greatest pressure reduction in the two gaps between the three blowing slots. For the intermediate car, all three blowing speeds elevate the negative pressure at that position, with the maximum blowing speed resulting in the largest pressure increase. This results in the fact that the lateral force of the intermediate car increases by 1.8% when the blowing speed is  $0.3U$ .

Streamlines projected onto X-slices are depicted in Fig. 18 to capture the variations in flow patterns resulting from the blowing velocity at a yaw angle of  $15^\circ$ . The positions of the slices are differentiated by columns, while the blowing speeds are differentiated by rows. The blowing velocity is unlikely to significantly affect the main vortex formation pattern on the leeward side of the train. However, it mainly influences the localized flow near the blowing slots due to the direct mixing of the normal ejected airflow with the airflow over the roof. The most noticeable difference occurs in the red-marked region, which is magnified in the upper-right corner. As the blowing speed increases, the active flow in this region becomes increasingly dominant in mixing with the origin flow, exhibiting a greater ability to form a normal flow. This implies an enhanced blocking effect, leading to a distinct variation

in flow distribution in the proximity region on the leeward side. Nevertheless, due to differences in the longitudinal position and the specific yaw angle, these variations in flow distribution do not exhibit a consistent change with increasing blowing speed.

### C. Mitigation efficiency assessment

Safety is of paramount importance for trains operating under crosswind conditions. As previously examined, the simultaneous application of air blowing to the head car, intermediate car, and tail cars proves effective in reducing the lateral force exerted on the train, thereby enhancing its safety in crosswind scenarios. This effect becomes more pronounced with increasing air-blowing speeds. However, the necessity of further increasing the air-blowing speed warrants careful consideration.<sup>34</sup> It analyzes the mitigating benefits of lateral aerodynamic forces experienced by the train at various blowing speeds, employing the lateral force  $C_y$  as the primary criterion. Furthermore, it evaluates an optimal air-blowing speed from the perspective of energy utilization rate, thus ensuring an appropriate balance between safety enhancement and efficient energy usage.

In order to evaluate the effect of the blowing strategy,  $\Delta F_y$  is introduced to represent the reduction in lateral force obtained by the entire train due to the application of the air-blowing, that is,

$$\Delta F_y = F_{y-0} - F_{y-1}. \quad (12)$$

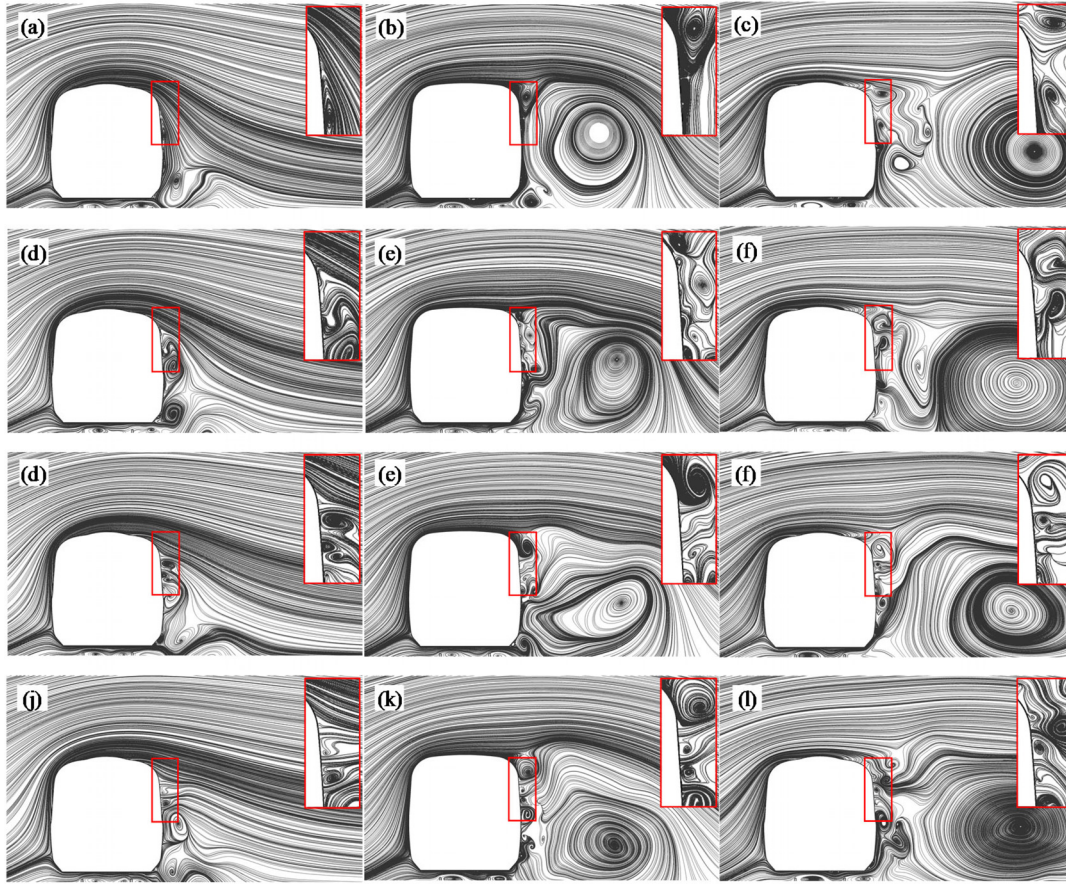


**FIG. 18.** Streamlines projected to X-slices in the  $\alpha = 15^\circ$  case: (a) prototype, X1, (b) prototype, X2, (c) prototype, X3, (d)  $v_b = 0.1U$ , X1, (e)  $v_b = 0.1U$ , X2, (f)  $v_b = 0.1U$ , X3, (g)  $v_b = 0.2U$ , X1, (h)  $v_b = 0.2U$ , X2, (i)  $v_b = 0.2U$ , X3, (j)  $v_b = 0.3U$ , X1, (k)  $v_b = 0.3U$ , X2, and (l)  $v_b = 0.3U$ , X3.

$F_{y-0}$  and  $F_{y-1}$  are the lateral forces acting on the origin train and the train with air-blowing, where the relation between the aerodynamic forces and their responding coefficients analyzed above can be found in Eqs. (1)–(3). In order to transform this indicator from the dimension of force to a more energy-efficient one, the product of  $\Delta F_y$  and the resultant velocity  $U$  are used to express it as the dimension of power, that is,

$$\Delta P_y = \Delta F_y \cdot U. \quad (13)$$

As a form of active control, the air blowing used in this work requires power related to its blowing speed and the area of the air-blowing slot, that is,

$$P_b = \frac{1}{2} \rho v_b^3 A_b, \quad (14)$$

where  $A_b$  is the area of the air-blowing slots. Active control is often a strategy that requires tradeoffs. In this work, if the power  $P_b$  consumed to generate active control can be reduced less than the equivalent power of the train's lateral force, it means that the current active control strategy is effective, using the indicator power return coefficient, defined as

$$\sigma = \frac{\Delta P_y}{P_b}. \quad (15)$$

To quantify the net power change of different air blowing strategies in different operating environments. A value less than 1 indicates that the air blowing strategy used will produce an overall energy loss, while a value greater than 1 proves that the current air blowing strategy is effective. Effectiveness means achieving higher value at less cost. Table III lists the  $\sigma$  values obtained by using different air blowing strategies for the entire train when operating at different yaw angles studied in this paper.

The current work still quantitatively describes the “cost-effectiveness” of the blowing strategy applied in different scenarios from the two perspectives analyzed previously. Under a same blowing speed of  $v_b = 0.2U$ , the power return coefficient  $\sigma$  for the entire train increases from 18.5 at a yaw angle of  $15^\circ$  to 234.2 at a yaw angle of  $45^\circ$  and then decreases to 34.8 at a yaw angle of  $75^\circ$ , proving that the same effort invested in blowing benefit at middle yaw angles the most, although substantial expected benefits can also be obtained at smaller and near  $90^\circ$  yaw angles. It is noteworthy that, at the same yaw angle, increasing the blowing speed from  $0.1U$  to  $0.3U$  always results in a decrease in the power return coefficient  $\sigma$ , despite the positive and

TABLE III. The power return coefficient  $\sigma$  for the air blowing strategies.

Items	The power return coefficient $\sigma$								
	15°			30°			75°		
	0.1U	0.2U	0.3U	0.2U	0.2U	0.2U	0.1U	0.2U	0.3U
$\alpha$									
$v_b$									
Head	−45.3	−4.3	0.1	4.0	26.3	111.6	334.9	35.4	12.9
Middle	56.2	9.9	4.2	5.8	114.0	33.0	−61.0	−2.6	−7.4
Tail	60.5	12.8	5.2	26.1	94.0	12.5	53.0	1.9	−2.3
Total	71.5	18.5	9.5	35.9	234.2	157.0	327.0	34.8	3.2

negative correlations of the overall lateral force shown at yaw angles of 15° and 75°, respectively. This highlights the higher returns of lower blowing speeds; therefore, a trade-off between absolute “performance” and relative “cost-effectiveness” shall be considered in practical applications.

Nonetheless, it must be pointed out that while the air blowing strategy mentioned in the present study does reduce the lateral forces on the train, given it is a way of ground transportation, air-blowing from the compartments might not be a realistic idea at this stage. Therefore, the author emphasizes that this is a potential method to improve the safety of train operations and has been proven to be reliable in theory. Exploring alternative methods or modifications that do not rely on air blowing from compartments might be worth considering.

In addition, there are some limitations of this study that need to be pointed out. Simplifications of the model used in numerical simulations (e.g., the replication of pantograph and vehicle cross-sectional shape) may affect the results of the study, although a localized effect is more likely to occur; the potential impact of scale modeling on applicability may exist due to differences in Reynolds number; and the uncertainty in some of the results also needs to be clarified such as the potential impact of train model and vehicle length.

IV. CONCLUSIONS

The current study employed the IDDES method based on the SST  $k-\omega$  turbulence model to investigate the mitigating effect of active air-blowing applied on the leeward side of the train on its aerodynamic forces. The application of this air blowing strategy at various yaw angles and using different blowing speeds were considered and examined. The primary findings are summarized as follows:

- (1) The application of air blowing strategy fundamentally alters the flow structure in the vicinity of the transition region from the top to the leeward side of the train, resulting in an increased turbulence level in the surrounding flow. This further leads to local-scale flow reconstruction near the air-blowing slots, which subsequently modifies the distribution of surface pressure.
- (2) The air-blowing slots have showcased their effectiveness in mitigating the aerodynamic lateral forces acting on each car. For the yaw angles ranging from 15° to 75° in 15° increments, the application of the air blowing strategy results in total reductions in lateral forces for the whole train of 4.7%, 3.1%, 8.8%, 4.3%, and 1.0%, respectively.

- (3) The effect of air-blowing speed on the lateral force reduction of the train is also sensitive to the yaw angle due to the complex train-crosswind-coupled flow field characteristics. With different blowing speeds, the total lateral force of the whole train is reduced by a maximum of 8.2% (for a yaw angle of 15°) and 1.1% (for a yaw angle of 75°).
- (4) The cost-effectiveness of air blowing was evaluated by defining the power return coefficient  $\sigma$ . The greatest reduction in lateral forces is achieved at middle yaw angles around 45°, while notable benefits can also be obtained at smaller and near 90° yaw angles. A higher blowing speed consistently leads to a decrease in the power return coefficient  $\sigma$ . A careful consideration of the trade-off between absolute performance and relative cost-effectiveness is essential in practical applications.

ACKNOWLEDGMENTS

This work was supported by a grant from the Research Grants Council of the Hong Kong Special Administrative Region (SAR), China (Grant No. 15205723), the National Natural Science Foundation of China (Grant No. 52202426), and a grant from The Hong Kong Polytechnic University (Grant No. P0045325). The authors would also like to appreciate the funding supported by the Innovation and Technology Commission of the Hong Kong SAR Government (Grant No. K-BBY1) and a grant from the Guangdong Basic and Applied Basic Research Foundation of Department of Science and Technology of Guangdong Province (Grant No. 2021B1515130006).

AUTHOR DECLARATIONS

Conflict of Interest

The authors have no conflicts to disclose.

Author Contributions

**Zi-Jian Guo:** Methodology (equal); Software (equal); Visualization (lead); Writing – original draft (lead). **Zheng-Wei Chen:** Conceptualization (lead); Methodology (equal); Resources (supporting); Supervision (equal); Writing – original draft (supporting). **Zheng-Xin Che:** Data curation (lead); Methodology (supporting); Software (supporting). **Amir Bordbar:** Investigation (supporting); Resources (supporting). **Yi-Qing Ni:** Funding acquisition (lead); Project administration (lead); Resources (lead); Supervision (equal).



## DATA AVAILABILITY

The data that support the findings of this study are available from the corresponding author upon reasonable request.

## REFERENCES

- <sup>1</sup>Z.-W. Chen, Z.-H. Guo, Y.-Q. Ni, T.-H. Liu, and J. Zhang, "A suction method to mitigate pressure waves induced by high-speed maglev trains passing through tunnels," *Sustainable Cities Soc.* **96**, 104682 (2023).
- <sup>2</sup>B. Yan, F. Yang, S. Qiu, J. Wang, B. Cai, S. Wang, Q. Zaheer, W. Wang, Y. Chen, and W. Hu, "Digital twin in transportation infrastructure management: A systematic review," *Intell. Transp. Infrastruct.* **2**, liad024 (2023).
- <sup>3</sup>Y. Zhang, D.-Z. Dang, Y.-W. Wang, and Y.-Q. Ni, "Damage identification for railway tracks using ultrasound guided wave and hybrid probabilistic deep learning," *Constr. Build. Mater.* **418**, 135466 (2024).
- <sup>4</sup>C. J. Baker, "The simulation of unsteady aerodynamic cross wind forces on trains," *J. Wind Eng. Ind. Aerodyn.* **98**(2), 88–99 (2010).
- <sup>5</sup>D. Zhou, C. Xia, L. Wu, and S. Meng, "Effect of the wind speed on aerodynamic behaviours during the acceleration of a high-speed train under crosswinds," *J. Wind Eng. Ind. Aerodyn.* **232**, 105287 (2023).
- <sup>6</sup>C. J. Baker, in *TRANSAERO—A European Initiative on Transient Aerodynamics for Railway System Optimisation* (Springer, Berlin, Heidelberg, 2002), pp. 46–60.
- <sup>7</sup>M. Boccione, F. Cheli, R. Corradi, S. Muggiasca, and G. Tomasini, "Crosswind action on rail vehicles: Wind tunnel experimental analyses," *J. Wind Eng. Ind. Aerodyn.* **96**(5), 584–610 (2008).
- <sup>8</sup>Z. Guo, T. Liu, Z. Liu, X. Chen, and W. Li, "An IDDES study on a train suffering a crosswind with angles of attack on a bridge," *J. Wind Eng. Ind. Aerodyn.* **217**, 104735 (2021).
- <sup>9</sup>Z. Guo, T. Liu, M. Yu, Z. Chen, W. Li, X. Huo, and H. Liu, "Numerical study for the aerodynamic performance of double unit train under crosswind," *J. Wind Eng. Ind. Aerodyn.* **191**, 203–214 (2019).
- <sup>10</sup>C. Baker, F. Cheli, A. Orellano, N. Paradot, C. Proppe, and D. Rocchi, "Crosswind effects on road and rail vehicles," *Veh. Syst. Dyn.* **47**(8), 983–1022 (2009).
- <sup>11</sup>Z. Chen, T. Liu, Z. Jiang, Z. Guo, and J. Zhang, "Comparative analysis of the effect of different nose lengths on train aerodynamic performance under crosswind," *J. Fluids Struct.* **78**, 69–85 (2018).
- <sup>12</sup>H. Hemida and S. Krajnović, "LES study of the influence of a train-nose shape on the flow structures under cross-wind conditions," *J. Fluids Eng.* **130**, 091101 (2008).
- <sup>13</sup>J. Muñoz-Paniagua and J. García, "Aerodynamic surrogate-based optimization of the nose shape of a high-speed train for crosswind and passing-by scenarios," *J. Wind Eng. Ind. Aerodyn.* **184**, 139–152 (2019).
- <sup>14</sup>H. Gu, T. Liu, Z. Jiang, and Z. Guo, "Research on the wind-sheltering performance of different forms of corrugated wind barriers on railway bridges," *J. Wind Eng. Ind. Aerodyn.* **201**, 104166 (2020).
- <sup>15</sup>M. Mohebbi and M. A. Rezvani, "2D and 3D numerical and experimental analyses of the aerodynamic effects of air fences on a high-speed train," *Wind Struct.* **32**(6), 539–550 (2021).
- <sup>16</sup>M. Mohebbi and M. A. Rezvani, "Two-dimensional analysis of the influence of windbreaks on airflow over a high-speed train under crosswind using lattice Boltzmann method," *Proc. Inst. Mech. Eng., Part F* **232**(3), 863–872 (2018).
- <sup>17</sup>G. Tomasini, S. Giappino, F. Cheli, and P. Schito, "Windbreaks for railway lines: Wind tunnel experimental tests," *Proc. Inst. Mech. Eng., Part F* **230**(4), 1270–1282 (2016).
- <sup>18</sup>Y. Xia, T. Liu, X. Su, Z. Jiang, Z. Chen, and Z. Guo, "Aerodynamic influences of typical windbreak wall types on a high-speed train under crosswinds," *J. Wind Eng. Ind. Aerodyn.* **231**, 105203 (2022).
- <sup>19</sup>S. F. Tardu and O. Doche, "Active control of the turbulent drag by a localized periodical blowing dissymmetric in time," *Exp. Fluids* **47**(1), 19–26 (2009).
- <sup>20</sup>W. Gao, X. Kong, Z. Deng, W. Yu, Y. Wu, and J. Luo, "Review of state of the art in active aerodynamic control research for vehicles," *J. Phys.: Conf. Ser.* **1985**(1), 012040 (2021).
- <sup>21</sup>Z.-W. Chen, Y.-Q. Ni, Y.-W. Wang, S.-M. Wang, and T.-H. Liu, "Mitigating crosswind effect on high-speed trains by active blowing method: A comparative study," *Eng. Appl. Comput. Fluid Mech.* **16**(1), 1064–1081 (2022).
- <sup>22</sup>X. Chen, S. Zhong, O. Ozer, and A. Weightman, "Control of afterbody vortices from a slanted-base cylinder using sweeping jets," *Phys. Fluids* **34**(7), 075115 (2022).
- <sup>23</sup>X. Chen, S. Zhong, O. Ozer, and A. Weightman, "Drag reduction of a slanted-base cylinder using sweeping jets," *Phys. Fluids* **34**(10), 105101 (2022).
- <sup>24</sup>Z.-X. Che, S. Huang, Z.-W. Li, and Z.-W. Chen, "Aerodynamic drag reduction of high-speed maglev train based on air blowing/suction," *J. Wind Eng. Ind. Aerodyn.* **233**, 105321 (2023).
- <sup>25</sup>S. Chegini, M. Asadbeigi, F. Ghafoorian, and M. Mehrpooya, "An investigation into the self-starting of Darrieus-Savonius hybrid wind turbine and performance enhancement through innovative deflectors: A CFD approach," *Ocean Eng.* **287**, 115910 (2023).
- <sup>26</sup>H. Gu, T. Liu, Z. Jiang, and Z. Guo, "Experimental and simulation research on the aerodynamic effect on a train with a wind barrier in different lengths," *J. Wind Eng. Ind. Aerodyn.* **214**, 104644 (2021).
- <sup>27</sup>Z. Guo, T. Liu, Y. Xia, and Z. Liu, "Aerodynamic influence of the clearance under the cowcatcher of a high-speed train," *J. Wind Eng. Ind. Aerodyn.* **220**, 104844 (2022).
- <sup>28</sup>Z. Guo, T. Liu, H. Hemida, Z. Chen, and H. Liu, "Numerical simulation of the aerodynamic characteristics of double unit train," *Eng. Appl. Comput. Fluid Mech.* **14**(1), 910–922 (2020).
- <sup>29</sup>K. He, X. Su, G. Gao, and S. Krajnović, "Evaluation of LES, IDDES and URANS for prediction of flow around a streamlined high-speed train," *J. Wind Eng. Ind. Aerodyn.* **223**, 104952 (2022).
- <sup>30</sup>K. Wang, X. Xiong, C. Wen, X. Li, G. Chen, Z. Chen, and M. Tang, "Impact of the train heights on the aerodynamic behaviour of a high-speed train," *Eng. Appl. Comput. Fluid Mech.* **17**(1), 2233614 (2023).
- <sup>31</sup>S. Farajyar, F. Ghafoorian, M. Mehrpooya, and M. Asadbeigi, "CFD investigation and optimization on the aerodynamic performance of a Savonius vertical axis wind turbine and its installation in a hybrid power supply system: A case study in Iran," *Sustainability* **15**(6), 5318 (2023).
- <sup>32</sup>F. Ghafoorian, S. R. Mirmotahari, F. Bakhtiari, and M. Mehrpooya, "Exploring optimal configurations for a wind farm with clusters of Darrieus VAWT, using CFD methodology," *J. Comput. Appl. Mech.* **54**(4), 533–551 (2023).
- <sup>33</sup>X.-S. Huo, T.-H. Liu, Z.-W. Chen, W.-H. Li, J.-Q. Niu, and H.-R. Gao, "Aerodynamic characteristics of double-connected train groups composed of different kinds of high-speed trains under crosswinds: A comparison study," *Alexandria Eng. J.* **64**, 465–481 (2023).
- <sup>34</sup>K. Xu, X. Su, R. Bensow, and S. Krajnovic, "Drag reduction of ship airflow using steady Coanda effect," *Ocean Eng.* **266**, 113051 (2022).